JPE 17-6-13

https://doi.org/10.6113/JPE.2017.17.6.1523
ISSN(Print): 1598-2092 / ISSN(Online): 2093-4718

Bus Clamping PWM Based Hysteresis Current Controlled VSI Fed Induction Motor Drive with Nearly Constant Switching Frequency

Joseph Peter*, Mohammed Shafi K P*, and Rijil Ramchand†

*,†Department of Electrical Engineering, National Institute of Technology, Calicut, India

Abstract

A Current Error Space Phasor (CESP) based hysteresis controller with online computation of the boundary for two-level inverter fed Induction Motor (IM) drives is presented in this paper. The stator voltages estimated along the α-and β-axes and the orthogonal current error components of the motor are used in the online computation of the hysteresis boundary. All of the inherent benefits of space phasor based hysteresis controllers such as its quick dynamic response and nearby voltage vector switching are present in the proposed scheme with the added benefit of suppressing switching frequency variations. The similarity in the frequency spectrum of the phase voltage obtained at the output of the inverter using the proposed scheme and Bus Clamping Pulse Width Modulation (BCPWM) based drive is justified with the help of extensive MATLAB SIMULINK simulations. The controller is experimentally verified with a three phase, 2.2 kW IM drive for steady state and transient conditions and the obtained results match the simulation results.

Key words: Current error space phasor, Hysteresis, Induction motor, Switching frequency

I. INTRODUCTION

Traditionally, Current Controlled Voltage Source Inverters (CCVSIs) are extensively employed for industrial and residential applications due to its simplicity, excellent dynamic response and intrinsic short-circuit protection [1]. In ac motor drives and active power filters, it is necessary to govern the current using a controller with current feedback. The quality of the employed current controller has the most significant impact on the overall performance of the closed loop control system. Therefore, inverter current control techniques have been able to grab the attention of researchers all over the world in the last few decades. To date, many classes of current controllers have emerged. The commonly used ones are the linear ramp-comparison control, hysteresis control, and predictive control [2].

Amongst these, the Hysteresis Current Controllers (HCCs) are the most desirable due to their simplicity, good accuracy and outstanding robustness. A conventional hysteresis controller adopts an independent controller for each phase of the load, and generates switching signals by comparing the recommended reference currents and the measured currents. Thus, it decides the switching state of the corresponding inverter leg of the VSI to keep the current within the hysteresis band [3]. However, while selecting the HCC as the best current controlling candidate for high performance drive operations, a price is being paid in terms of variable inverter switching frequency, random switching and non-optimum current ripple. Various proposals have been suggested in the literature to overcome the constraints of hysteresis regulators [4]-[14]. One suggestion is to have a variable hysteresis band for a continuously varying current. Here, the derivative of the output current error and the inverter switching states are used to maintain a constant switching frequency. However, the derivative of the current error is vulnerable to high frequency noise, particularly at higher switching frequencies [4]. Another strategy adopted is to enumerate the desired hysteresis band variation to synchronize the current error zero crossings to an external clock [4], [5]. However, issues in the computation of the band can degenerate the regulator's overall performance.

An adaptive hysteresis band and sinusoidal band current control has been proposed to maintain a fixed switching

Manuscript received Apr. 8, 2017; accepted Aug. 12,2017
Recommended for publication by Associate Editor Zheng Wang.
†Corresponding Author: rijil@nitc.ac.in
Tel: +91-944-602-0078, Fax: +91-495-228-7250, Nat'l Inst. Tech.
*Dept. of Electrical Engineering, National Institute of Technology, India

frequency and to discard the interphases dependency [5]. However, they both steadily go through stability problems and constricted transient performance which results in current distortion. Several modified configurations have been presented by various research groups to improve the performance of the HCC such as suppressing the limit cycle variations as presented in [6].

To mitigate the issues caused by earlier HCCs and to get a controlled switching frequency in two-level VSI fed IM drives, a space vector based hysteresis controller was introduced in [7]. It operates on the CESP, which deals with the combined effect of the current error on three phases of an IM with different shapes of the error boundary as circular, rectangular and hexagonal etc. [7]-[15]. The CESP is kept within the boundary by utilizing the switching of the zero or nonzero inverter voltage vector whenever it tries to go out of the specified boundary. The controller is capable of obtaining the desired control of the switching frequency variation to some extent, independent of load motor parameters [7]-[10]. However, a nearly constant switching frequency is possible if the hysteresis current error boundary is similar to that of the constant switching frequency Voltage Controlled Space Vector PWM (VC SVPWM). To achieve this, an innovative online variation of the parabolic boundary for the current error space phasor, depending on the operating speed, is suggested for the first time in [8]. The hysteresis controller pre-calculates the boundary of the CESP using the leakage inductance of the given induction motor and comes up with a switching frequency spectrum of the inverter output voltage that is identical to that of the constant switching frequency VC-SVPWM based VSI fed IM drive. The requirement of an outer parabola for a sector change and the introduction of harmonics into the voltage and current results in a degraded performance of the drive, especially in low speed operations. The method proposed in [9] overcomes the previous limitations by using current errors along the orthogonal axes to detect sector changes. In [10], the parabolic current error boundaries reported in [8], [9] are replaced with a simple online computation of the required boundaries. A method for estimating the stator voltages and identifying the present sector is also proposed in [10]. Several studies have reported the possibility of facilitating the use of zero vectors along with active vectors in Space Vector Modulation (SVM) techniques with hysteresis controller strategies, to obtain a controllable switching frequency. The SVM technique also contributes to a nearly 15% higher DC bus utilization and an improved performance when compared to that of the sinusoidal PWM technique and the conventional HCC [16]-[18]. Furthermore, a reduction in the switching losses can be realized by combining the SVPWM with the bus clamping technique popularly known as the bus clamping SVPWM or discontinuous PWM [18].

A CESP based hysteresis controllers incorporating the advantages of BCPWM for constant frequency operations has not been addressed or analyzed so far. In the proposed method, the controller ensures adjacent voltage vectors switching in a given sector of the voltage space phasor, and ignores the picking of arbitrary voltage vectors. The fundamental stator voltage estimated using the current error along the alpha and beta axis are used for the sector selection, the dwell time calculation of the voltage vectors and the online computation of the hysteresis boundary [9]-[14], [18]. The performance of the proposed controller is replicated in the MATLAB Simulink platform and a detailed analysis is done. The proposed method shows that the CESP boundaries and switching frequency variations in a fundamental cycle and over the entire speed range are similar to those of a constant switching frequency voltage controlled bus clamping PWM based VSI fed IM drive. All of the other inherent advantages of space phasor based hysteresis controllers like optimal voltage vector switching and better dynamic response are retained in the proposed scheme along with the elimination of switching frequency variations, which makes the drive suitable for precise control operations. The steady state and transient performance of the proposed current controller are implemented with the RTI-1103 dSPACE platform and experimentally tested on a 2.2 kW IM drive.

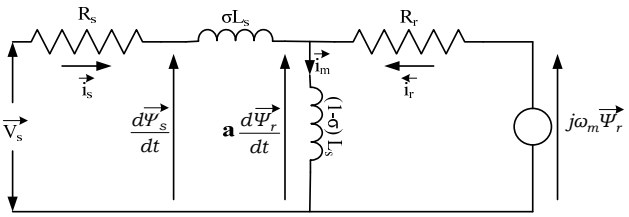

Fig. 1. Space phasor based equivalent circuit of an IM drive with the rotor flux as a reference vector [10].

This paper is organized as follows. The mathematical equations of the CESP based hysteresis current controller are reviewed in Section 2. Computation and analysis of the current error boundary and the effect of parameter variations for the proposed controller are presented in Section 3. Simulation and experimentation results with the proposed controller strategy are illustrated in Section 4. A comparison of controllers and some conclusions are given in Section 5 and Section 6, respectively.

II. CESP Based Hysteresis Controller

In the CESP based hysteresis controller, whenever the CESP goes outside the predefined boundary, an appropriate inverter voltage vector that brings the current error back inside the boundary is switched. The boundary computed in the present sampling interval is used for identifying next vector to be switched. This is carried out using the estimated magnitude ($|V_s|$) and position (α) of the fundamental stator voltage vectors (V_s). The estimated values of $V_{s\alpha}$ and $V_{s\beta}$ are used for computing the sector in which V_s is lying. $V_{s\alpha}$ and

$V_{s\beta}$ are converted to three phase voltages and from this the voltage vector switching times used for the boundary computations are calculated.

A. Estimation of the Fundamental Stator Voltage

The Fig. 1 shows a steady state equivalent circuit of an IM in the stator reference frame with the rotor flux as a reference vector. Applying Kirchhoff Voltage law, the stator voltage vector V_s equation can be derived from Fig. 1.

$$\vec{V}_s=\vec{i}_sR_s+\sigma L_s\frac{d\vec{i}_s}{dt}+a\frac{d\vec{\Psi}_r}{dt}=\vec{i}_sR_s+\sigma L_s\frac{d\vec{i}_s}{dt}+\vec{V}_r \quad (1)$$

$$\vec{V}_s=\vec{i}_sR_s+\frac{d\vec{\Psi}_s}{dt},where\vec{\Psi}_s=\sigma L_s\vec{i}_s+\vec{V}_m=\sigma L_s\vec{i}_s+a\vec{\Psi}_r \quad (2)$$

Here, ψ_s = stator flux vector, ψ_r = rotor flux vector, R_s = stator resistance, σL_s = leakage inductance of the IM, L_m = magnetising inductance, L_s and L_r = self-inductances of the stator and rotor, respectively, and a=Lm/Lr. Here, $i_s=i_s*+\Delta i_s$, where i_s* = reference current space phasor, and Δi_s = current error space phasor. From (2), it is possible to obtain an expression for the fundamental rotor voltage vector V_r in terms of the applied inverter voltage vectorV_k and reference current vector i_s* as shown in (3).

$$\vec{V}_r=\left(\vec{V}_k-(\vec{i}_s^{\,*}R_s+\sigma L_s\frac{d\vec{i}_s^{\,*}}{dt})-(\Delta\vec{i}_sR_s+\sigma L_s\frac{d\Delta\vec{i}_s}{dt})\right) \quad (3)$$

In (3), the applied voltage vector is V_k, (k varies from 1 to 8 according to the switching of the active and zero vectors) as in Fig. 2. From the fundamental rotor voltage vector it is possible to obtain the fundamental stator voltage V_s vector by adding the fundamental voltage drop across the stator resistance and stator leakage inductance as shown in (4).

$$\vec{V}_s=\left(\vec{V}_r+(\vec{i}_s^{\,*}R_s+\sigma L_s\frac{d\vec{i}_s^{\,*}}{dt})\right) \quad (4)$$

By combining (3) and (4), the fundamental stator voltage vector can be rewritten as (5).

$$\vec{V}_s=\left(\vec{V}_k-(\Delta\vec{i}_sR_s+\sigma L_s\frac{d\Delta\vec{i}_s}{dt})\right) \quad (5)$$

Equation (5) can be expressed as two equations in the α-axis and β-axis, as shown in Fig. 2. Therefore, using Δis_α, Δis_β, $V_{k\alpha}$, and $V_{k\beta}$, it is possible to estimate the values of $V_{s\alpha}$ and $V_{s\beta}$. During the active vector periods, V_k can be any one of the six active vectors and the expression for the fundamental stator voltage vector is modified as the equations shown in (6) and (7).

$$\vec{V}_{s\beta}=\left(\vec{V}_{k\beta}-(\Delta\vec{i}_{s\beta}R_s+\sigma L_s\frac{d\Delta\vec{i}_{s\beta}}{dt})\right) \quad (6)$$

$$\vec{V}_{s\alpha}=\left(\vec{V}_{k\alpha}-(\Delta\vec{i}_{s\alpha}R_s+\sigma L_s\frac{d\Delta\vec{i}_{s\alpha}}{dt})\right) \quad (7)$$

In (6) and (7), the effect of the change of the stator resistance r_s due to temperature variations is inconsiderable, since the term with σL_s dominates the other. The time duration of the null vectors is more than time duration of the active vectors when the frequency is less than 25 Hz. Once the frequency is more than 25 Hz, the time duration of the active vectors is more than the zero vectors. Therefore, when the frequency of operation is less than 25 Hz, it is possible to estimate the fundamental stator voltage vector exactly during the zero vector periods itself. However, once the frequency is more than 25 Hz, it is necessary to estimate the fundamental stator voltage vector during the active vector periods to get accurate results.

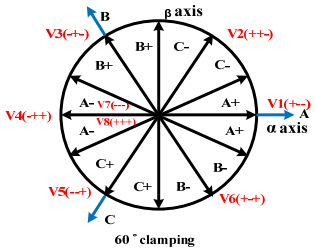

Fig. 2. Vector states and clamping phases of 60˚ BCPWM.

TABLE I
SECTOR SELECTION LOGIC

Present sub sector	Present vector	Cos α	Sin α	Next sub sector
1	V_2 or V_8	<=0.866	>=0.5	2
2	V_2 or V_7	<=0.5	>=0.866	3
3	V_3 or V_7	<0	>= 0.99	4
4	V_3 or V_8	<=-0.5	<=0.866	5
5	V_4 or V_8	<=-0.866	<=0.5	6
6	V_4 or V_7	<= -0.99	<0	7
7	V_5 or V_7	>=-0.866	<=-0.5	8
8	V_5 or V_8	>=-0.5	<=-0.866	9
9	V_6 or V_8	>0	<= 0.99	10
10	V_6 or V_7	>=0.5	>=-0.866	11
11	V_1 or V_7	>=0.866	>=-0.5	12
12	V_1 or V_8	>= 0.99	>0	1

During the zero vector period, the value of the instantaneous voltage vector is zero and the equation can be modified as:

$$\vec{V}_{s\alpha}=\left(-(\Delta\vec{i}_{s\alpha}R_s+\sigma L_s\frac{d\Delta\vec{i}_{s\alpha}}{dt})\right) \quad (8)$$

$$\vec{V}_{s\beta}=\left(-(\Delta\vec{i}_{s\beta}R_s+\sigma L_s\frac{d\Delta\vec{i}_{s\beta}}{dt})\right) \quad (9)$$

B. Identification of Sector

The sector identification, which gives us an idea about the stator voltage reference vector location, is used for calculating the current-error boundary and to realize the conditions for the adjacent voltage vector switching.

$$|V_s|=\sqrt{V_{s\alpha}^2+V_{s\beta}^2} \quad (10)$$

$$\cos\alpha=\frac{V_{s\alpha}}{|V_s|} \quad (11)$$

The reference voltage vector V_s sweeps 12 sub sectors, of 30˚ each, to complete one revolution of the fundamental stator voltage vector. The sector detection logic of 12 subsectors is explained in Table I.

C. Computation of Vector Dwell Times

The three phase voltages, V_a, V_b and V_c, are calculated from $V_{s\alpha}$ and $V_{s\beta}$ using an inverse-Clarke transformation. For each sector, for the set of three voltages, V_a, V_b, and V_c, the maximum (Max V), minimum (Min V) and the intermediate (Inter V) voltages are classified. These are used for calculating the active (T_1,T_2) and zero vector (T_0) timings. In the SVPWM, every reference voltage vector in all of the sectors can be formed by combining two adjacent active space vectors (1 to 6) and the null-state vectors 7 and 8 for a specific amount of a sampling period T_s. The timing intervals of the vectors are as follows:

$$T_1 = \frac{MaxV - InterV}{V_{dc}} T_s \quad (13)$$

$$T_2 = \frac{InterV - MinV}{V_{dc}} T_s \quad (14)$$

$$T_0 = T_s - (T_1 + T_2) \quad (15)$$

Inverter output voltage with a low harmonic content is obtained by SVM based on the volts second balance. However, this results in switching distortions. This can be reduced by clamping any one phase at a time to the positive or negative dc bus terminals for a finite span to procure the reference voltage vector, which is known as bus clamping SVM (BC SVM) [16]-[18]. The clamping duration of the phases depends on the vector switching for the allocation of the reference voltage vector results in:

- 60° bus clamping where each motor phase clamps for a 60° span in every half cycle of the reference voltage;
- 30° bus clamping where each motor phase clamps for a 30° span in every quarter cycle of the reference voltage [17].

III. Analysis of the Current Error Space Phasor

In the CESP based controller, when a voltage vector is switched, the instantaneous current error Δi travels in a direction depending upon the present vector and touches the hysteresis boundary. The current error is monitored along all of the six directions normal to phases A, B, C (jA, jB, jC, –jA, –jB, –jC). Here, whenever a CESP goes outside the boundary, the voltage vector which brings the current error back inside the boundary will be switched.

A. CESP Trajectory

The instantaneous voltage error vectors in the six sectors for various positions of the reference voltage vector V_s^* are as given in Fig.3. Considering that the first sector, V_s^* (OR) is inclined to the α axis at an angle alpha(α), and RA, RB and RR' are the directions of the CESP for vector switching V_1, V_2 and V_0, respectively. In ΔAOB, V_s^* can lie at α, where 0<α<60°. In sector 1, when V_1 is switched, if V_s^* is at 0°, the CESP moves in the direction of OA. If it is at 60°, the CESP travels in the

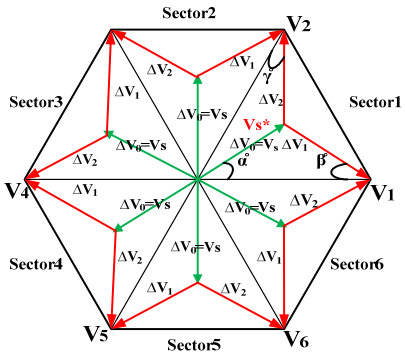

Fig. 3. Instantaneous voltage and current error vectors.

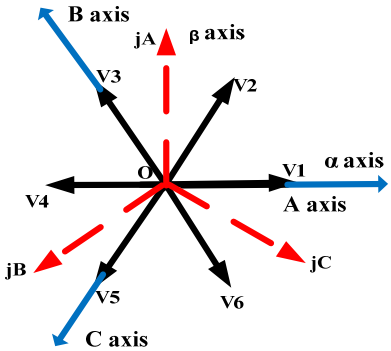

Fig. 4. Orthogonal axes for current error monitoring.

TABLE II
Orthogonal Axes for Vector Change Detection

Sector	Switching vectors	Orthogonal axes for vector change detection
1	1	jC
	2	jA
	7, 8	jB

direction of BA parallel to OF. Therefore, when V_1 is switched, the movement of Δi is bounded within two directions of OA and OF for any positions of V_s^*.

Similarly, for any position of V_s* within sector-1, when the vectors V_2, V_0 are switched, the directions in which Δi can move are confined to within the two directions OC and OB & OD and OE, respectively [8]. The switching of V_1 causes Δi to move along the jC axis as in Fig. 4. When V_1 switches, the maximum variation of the current error phasor can be monitored along the jC axis. Similarly, it is possible to identify an orthogonal-axis with the maximum deviation in the current error for all of the vectors as in Table II [10].

Considering sector 1 in Fig. 3, applying the parallelogram law of vector addition, the instantaneous voltage error vectors are calculated as below. These voltage errors are used for determining the instantaneous current errors.

$$\left|\Delta \vec{V}_1\right| = \sqrt{V_{dc}^2 + V_s^2 - 2V_1V_s\cos\alpha} \quad (16)$$

$$\left|\Delta \vec{V}_2\right| = \sqrt{V_{dc}^2 + V_s^2 - 2V_2V_s\cos\left(60^\circ - \alpha^\circ\right)} \quad (17)$$

$$\left|\Delta \vec{V}_0\right| = V_s \quad (18)$$

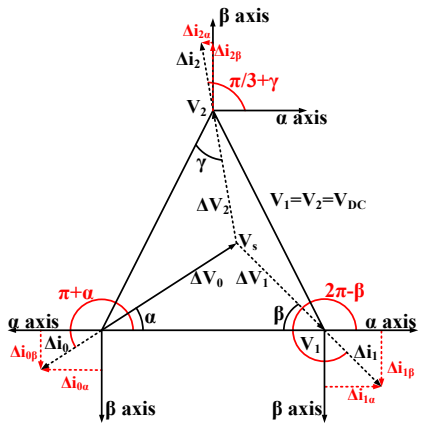

Fig. 5. Current error boundary computation diagram.

B. Computation of the Current Error Boundary

The voltage and current equation for a three-phase VSI fed IM is given by (19), where, V_k is the inverter voltage vector (k can be any number from 1 to 8),

$$\vec{V}_k = \vec{i}_s R_s + \sigma L_s \frac{d\vec{i}_s}{dt} + \vec{V}_r \tag{19}$$

From the voltage equation in (19), it is possible to obtain an expression for the rate of change of the current error in terms of the stator leakage inductance σL_s and the instantaneous voltage error ΔV, where ΔV is the difference between the applied voltage vector V_k and the fundamental stator voltage vector V_s.

$$\Delta i_1 = \frac{\Delta V_1}{\sigma L_s} T_1 \tag{20}$$

$$\Delta i_2 = \frac{\Delta V_2}{\sigma L_s} T_2 \tag{21}$$

$$\Delta i_0 = \frac{\Delta V_0}{\sigma L_s} T_0 \tag{22}$$

From the current error phasor diagram shown in Fig. 5, by using mathematical trigonometry, the components of Δi_1, Δi_2 and Δi_0 along the α and β axes are computed. The generalized equations of the α-β components of the current errors depending upon the sector (n=1 to 6) in which the stator voltage vector lies are shown below.

$$\Delta i_{0\alpha} = \Delta i_0 cos(180° + \alpha^\circ) \tag{23}$$

$$\Delta i_{0\beta} = \Delta i_0 sin(180° + \alpha^\circ) \tag{24}$$

$$\Delta i_{1\alpha} = \Delta i_1 cos((n-1) * 60° - \beta^\circ) \tag{25}$$

$$\Delta i_{1\beta} = \Delta i_1 sin((n-1) * 60° - \beta^\circ) \tag{26}$$

$$\Delta i_{2\alpha} = \Delta i_2 cos(n * 60° + \gamma^\circ) \tag{27}$$

$$\Delta i_{2\beta} = \Delta i_2 sin(n * 60° + \gamma^\circ) \tag{28}$$

The orthogonal-axes components of Δi_1, Δi_2 and Δi_0 are obtained using the transformation shown in (29). These are used for calculating the current-error boundary for the vectors V_1, V_2 and V_0 [10] and they are used for the vector selection logic in the proposed controller.

$$\begin{bmatrix} \Delta i_{xjA} \\ \Delta i_{xjB} \\ \Delta i_{xjC} \end{bmatrix} = \begin{bmatrix} 0 & 1 \\ \frac{-\sqrt{3}}{2} & -\frac{1}{2} \\ \frac{\sqrt{3}}{2} & -\frac{1}{2} \end{bmatrix} * \begin{bmatrix} \Delta i_{x\alpha} \\ \Delta i_{x\beta} \end{bmatrix} \qquad x=0,1,2. \tag{29}$$

TABLE III
VECTOR SELECTION LOGIC

Present sub sector	Present vector	axis	Previous vector	Next vector		
				jIa-(jIa*+ΔI$_{2ja}$/2)≥0	jIb-(jIb*+ΔI$_{0jb}$/2)≥0	jIc-(jIc*+ΔI$_{1jc}$/2)≥0
1(0°-30°) 821-128	8	jB	-	-	2	-
	2	jA	8	1	-	-
			1	8	-	-
	1	jC	-	-	-	2
2(30°-60°) 712-217	7	jB	-	-	1	-
	8	jB	-	-	2	-
	1	jC	7	-	-	2
			2	-	-	7
	2	jA	-	1	-	-

C. Vector Selection Logic

Precise sector detection and vector selection in the voltage space vector diagram are needed to control the machine current in the proposed controller. The 821-128(0°-30°) and 712-217(30°-60°) sequences are used in subsectors 1 and 2 which results in 60° bus clamping. Once the current error boundary along the orthogonal axes jA, jB and jC for all of the vectors in a sector are computed, half of the computed boundary values are added to the reference current along that particular orthogonal axis, which acts as the actual boundary for the current. When a vector is switched, the orthogonal axis with the maximum current error variation is monitored. When it reaches the boundary value, depending upon the present sector, present vector and previous vector, the next vector will be decided as shown in Table III to bring back the current error within the boundary. In the first sub sector, if the present switching vector is 2, the current error variation is monitored in the jA axis untill it reaches boundary of jIa*+Δi_{2ja}/2. If the previous vectors is 8, vector 1 will be applied next to control the current error. If the previous vector is 1, the next vector applied is 8. This way, apart from the current control, the proposed controller is able to maintain adjacent vector switching that is similar to that of the SVPWM.

D. Effect of the Stator Resistance (R_s) on the System Parameters

The effect of the stator resistance, (R_s) variation on the system parameters is evaluated with the simulation model before conducting experiments for different load torque conditions. The stator resistance, R_s has been increased up to 20% of the actual value of R_s in 10% steps. Fig. 6 shows the variation of the relative error in using R_s for the the estimation of the fundamental stator voltage V_s.

Relative error=(x-y)/y where:

x=estimated value of V_s with R_s,

y=estimated value of V_s without R_s.

The relative error is very small at less than 5%, as shown in Fig. 6. Therefore, the effect of stator resistance in the

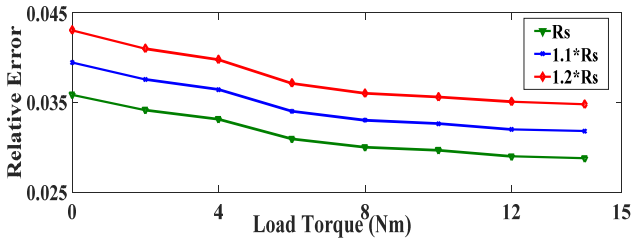

Fig. 6. Effect of stator resistance variation.

estimation of the fundamental stator voltage can be neglected.

E. Estimation of the Leakage Inductance (σL_s)

For calculating the leakage inductance, (5) can be rewritten as:

$$\vec{V}_k - \vec{V}_s = \left(\Delta\vec{i}_s R_s + \sigma L_s \frac{d\Delta\vec{i}_s}{dt} \right) \quad (30)$$

The fundamental stator voltage Vs can be assumed to be constant during two adjacent output voltage space vectors. This assumption can be made since the leakage time constant of an IM is much greater than the PWM switching period. Therefore, the value of V_s can be eliminated from (30). Hence, during vector 1, (30) can be written as:

$$\vec{V}_{k1} - \vec{V}_s = \left(\Delta\vec{i}_{s1} R_s + \sigma L_s \frac{d\Delta\vec{i}_{s1}}{dt} \right) \quad (31)$$

During vector 2, (30) can be written as:

$$\vec{V}_{k2} - \vec{V}_s = \left(\Delta\vec{i}_{s2} R_s + \sigma L_s \frac{d\Delta\vec{i}_{s2}}{dt} \right) \quad (32)$$

Now eliminating V_s from (31) and (32), the following can be obtained:

$$\vec{V}_{k1} - \vec{V}_{k2} = \left((\Delta\vec{i}_{s1} - \Delta\vec{i}_{s2}) * R_s + \sigma L_s \left(\frac{d\Delta\vec{i}_{s1}}{dt} - \frac{d\Delta\vec{i}_{s2}}{dt} \right) \right) \quad (33)$$

Since the effect of variations of R_s for the estimation of V_s is small, the stator resistance drop can be neglected in comparison with the leakage inductance drop.

$$\vec{V}_{k1} - \vec{V}_{k2} = \left(\sigma L_s \left(\frac{d\Delta\vec{i}_{s1}}{dt} - \frac{d\Delta\vec{i}_{s2}}{dt} \right) \right) \quad (34)$$

Hence, the leakage inductance can be estimated using:

$$\sigma L_s = \frac{\vec{V}_{k1} - \vec{V}_{k2}}{\frac{d\Delta\vec{i}_{s1}}{dt} - \frac{d\Delta\vec{i}_{s2}}{dt}} \quad (35)$$

Equation (35) is used to estimate the leakage inductance σL_s for simulation and experimental studies during steady-state operation. This scheme is used for updating the value of σL_s online and the updated value of σL_s is used in (6), (7), (8) and (9) for estimating the stator voltages and for computing the current-error boundary. The equation is solved for two consecutive vectors. It can be two active vectors, or one active vector and one zero vector, where V_{k1}, stands for the first vector, and V_{k2} stands for the second vector. The rate of change of the CESP is calculated using two samples of the current error during the same vector periods. Hence, the value of the leakage inductance is estimated using only the current error and the sensed dc-link voltage. The calculated value of the leakage inductance is filtered with a low-pass filter with a cutoff frequency of 1 kHz.

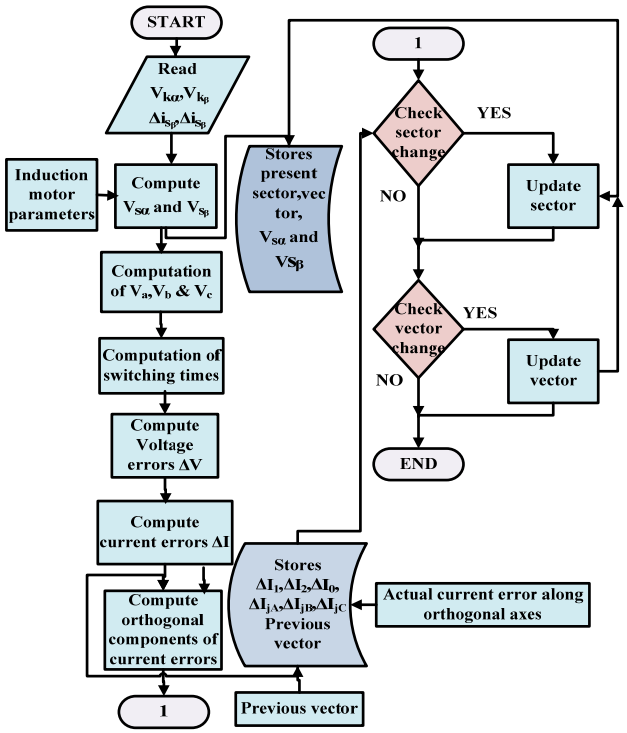

Fig. 7. Flow chart of the proposed control algorithm.

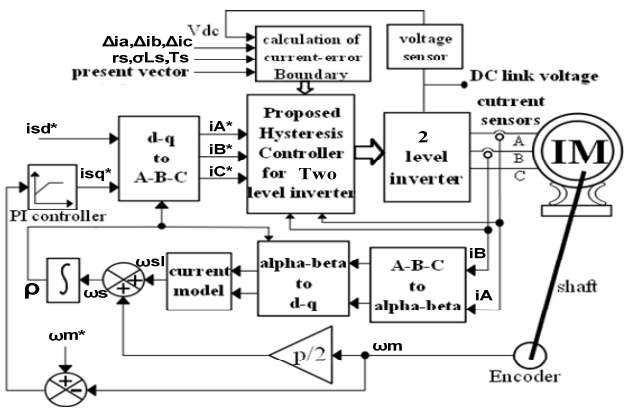

(a)

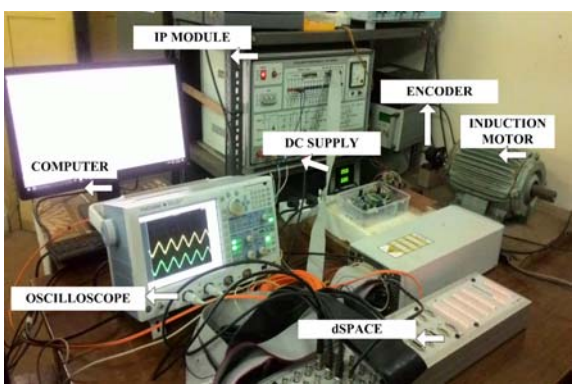

(b)

Fig. 8. (a) Block diagram. (b) Experimental set up of the control.

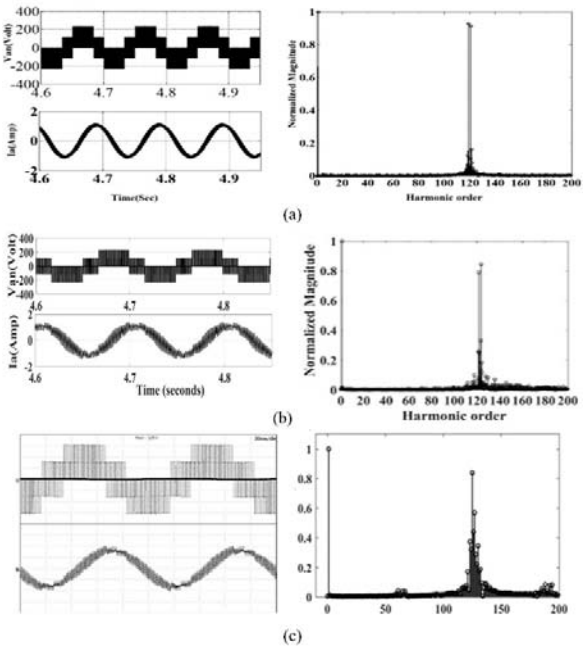

Fig. 9. Phase voltage along with the phase current and phase voltage harmonic spectrum (x axis: harmonic order; y axis: normalized harmonic amplitude) of an IM drive with: (a) VC; (b) proposed CC simulated; (c) proposed CC experimental [Y: upper trace:1 div=80V, lower trace:1 div=0.5A, X: 1 div=0.020s] at 10Hz.

IV. Simulation and Experimentation Results

Experimental verfication of the proposed CESP based hysteresis controller is carried out using a 2.2 kw 3 phase, star connected, induction motor drive, (the motor parameters are shown in Appendix A) fed from a 2 level VSI using vector control with a dSPACE 1103 platform. A flowchart of the proposed algorithm is shown in Fig. 7. A detailed block diagram and the experimental setup of the proposed controller based IM drive are shown in Fig. 8. The speed of the accelerating motor is sensed with an quadrature position encoder with 1024 ppr. The phase currents and voltage are sensed using LTS25P current sensors and LEM voltage sensors LV25-P. Simulations have been carried out for the proposed control in the MATLAB SIMULINK platform. The speed controller is executed at every 800 μsec and the current is sampled at every 10 μsec.

The phase voltage and phase current of the proposed current controller at various speeds of operation are simulated as shown in Fig. 9, Fig. 10 and Fig. 11. In additon, the corresponding harmonic spectrums of the phase voltage are also given (normalized to the base with an amplitude at the fundamental frequency). Fig. 9(c), Fig. 10(b) and Fig. 11(b) show the steady state phase voltage and phase current obtained during experimentation at 10Hz, 20Hz and 30Hz, respectively. Simulation and experimental results with spectrum frequencies show that the proposed current controller (CC) is able to attain a nearly constant switching

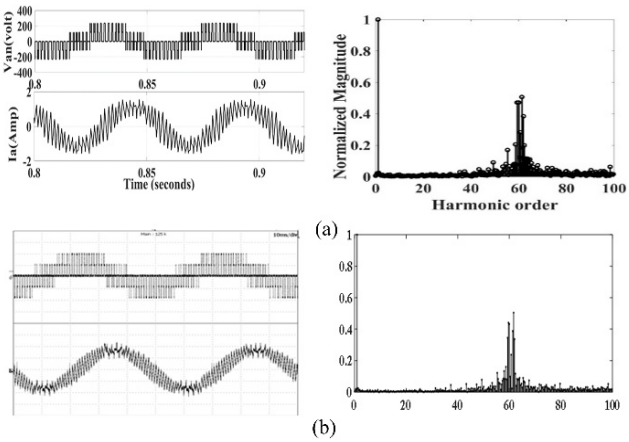

Fig. 10. Phase voltage along with phase current and phase voltage harmonic spectrum (x axis: harmonic order; y axis: normalized harmonic amplitude) of an IM drive with the proposed CC: (a) simulated (b) experimental [Y: upper trace:1 div=120V, lower trace:1 div=0.5A, X:1 div=0.010s] at 20Hz.

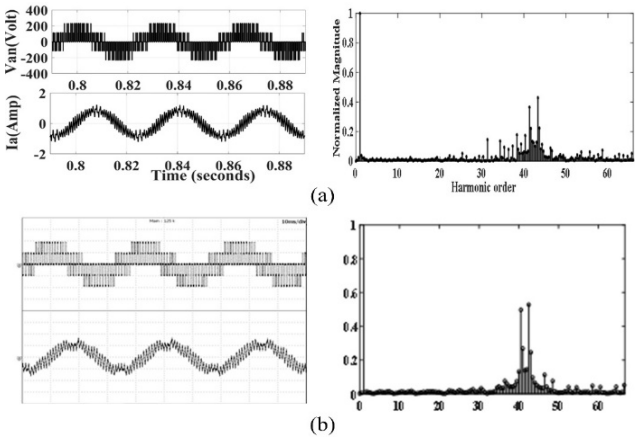

Fig. 11. Phase voltage along with phase current and phase voltage harmonic spectrum (x axis: harmonic order; y axis: normalized harmonic amplitude) of an IM drive with the proposed CC: (a) simulated; (b) experimental [Y: upper trace:1 div=120V, lower trace:1 div=1A, X:1 div=0.010s] at 30Hz.

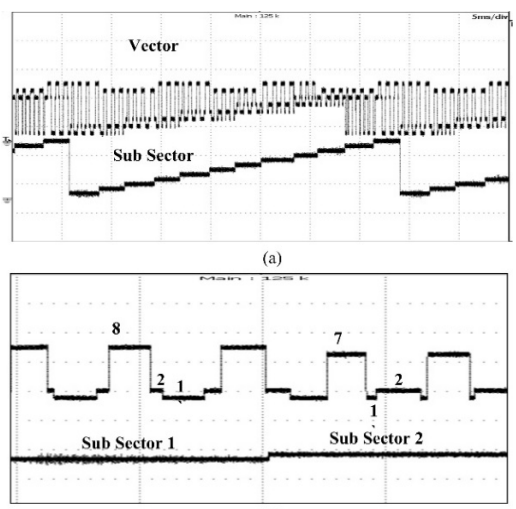

Fig. 12. (a) Vector (1 to 8) and sub sector (1 to 12). (b) Zoomed view of vectors 821-128 and 712-217 in sub sectors 1 and 2 with the proposed hysteresis controller (experimental results).

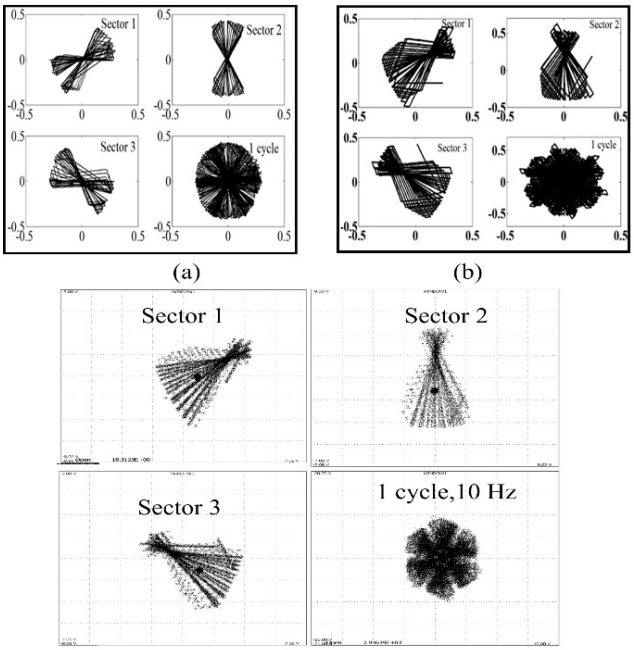

Fig. 13. CESP for sectors 1, 2, 3 and one fundamental cycle at 10Hz for: (a) VC; (b) proposed CC simulated; (c) proposed CC experimental (Y: 0.5 A/div, X-: 0.5 A/div).

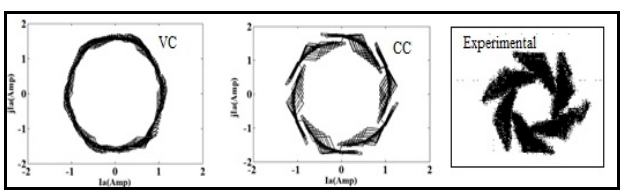

Fig. 14. Current Space Phasor (CSP) for the VC, the proposed CC (simulated) and the proposed CC (experimental) at 10 Hz (Y: 1A/div; X:1 A/div)

frequency (i.e. 1250 Hz for T_s=0.0008 sec) that is similar to that of the constant switching VC SVPWM, which is evident from the phase voltage FFTs.

Fig. 12(a) shows the switching vectors in 12 sub sectors at 30 Hz and Fig. 12(b) gives a zoomed in view of the vectors switching in sector 1 respectively. The 8-2-1-1-2-8 and 7-1-2-2-1-7 switchings in sub sectors 1 and 2, ensure the adjacent voltage vector switching in the proposed CESP based IM drive.

The trajectory of the current error space phasor in different sectors at various frequencies are investigated in the VC and the proposed CC IM drive. The trajectory of the CESP can be approximated to a parabola with a CSVPWM controller [8], whereas nearly triangular boundaries are formed when a BCPWM controller is used. Simulated and experimental X-Y plots of the alpha beta current errors for sectors 1, 2, 3 and for one fundamental cycle at the 10 Hz operation of an IM drive are shown in Fig. 13. The simulated and experimental results of the proposed current controller in Fig. 13(b) and Fig. 13(c) show that the current error trajectory pattern is similar to that of the error boundaries, shown in Fig. 13(a),

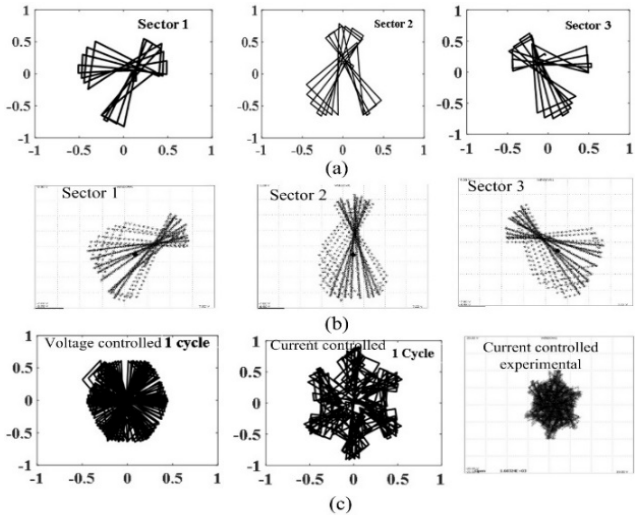

Fig. 15. CESP of sector 1,2 & 3 at 30 Hz with proposed CC IM drive (a) simulated (b) experimental (c) CESP of 1 fundamental cycle with IM drive at 40 Hz; Simulated (Voltage & proposed CC)& Experimental proposed CC result [Y:0.5A/div,X:0.5A/div].

with the VC BC SVPWM control. This verifies the concept of the constant switching frequency for the proposed controller. Fig. 14 shows the trajectory of current space phasor for one fundamental cycle at 10 Hz in the VC and the proposed CC IM drive. Fig. 15(a) and Fig. 15(b) show the simulated and experimental CESP for sectors 1, 2 and 3 at 30 Hz operation with the proposed CC drive. It can be observed from the results that the shape of the CESP boundary in the current controlled IM drive for a given opearting speed is same for all of the sectors, but with different current space phasor orientations. For all the sectors, the current error boundary looks similar to that of their respective diagonal sectors such as Sector 1 and Sector 4, Sector 2 and Sector 5, and Sector 3 and Sector 6. An intense examination of mentioned current error plots shows that the hysteresis controller proposed here retains Δi within the predetermined boundaries. All of the experimental plots of the boundary of Δi in the steady state are in unison with the simulation results. The steady state three phase currents and the phase current variations with different load torques at 20 Hz in the proposed current controlled IM drive are shown in Fig. 16(a) and Fig. 16(b), respectively. Fig. 16(c) gives the transient behaviour of the machine current and speed while accelerating from a steady state to a standstill at 20 Hz in proposed current controlled IM drive. Fig. 16(d) shows the motor speed, phase current and phase voltage during a speed reversal of an IM from 20 Hz to -20 Hz using the proposed controller at 0.75 seconds. Fig. 17(a) gives the transient behaviour of the machine phase voltage and current while a sudden change in I_{sq} is applied in the proposed current controlled IM drive. Fig. 17(b) shows that the CESP based controller has a fast dynamic response when the machine current is tracking the reference current during transients. The

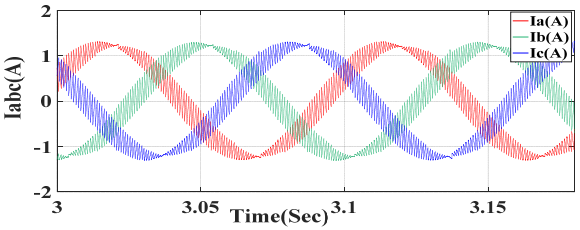

(a)

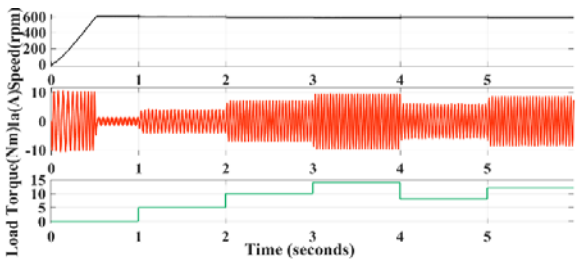

(b)

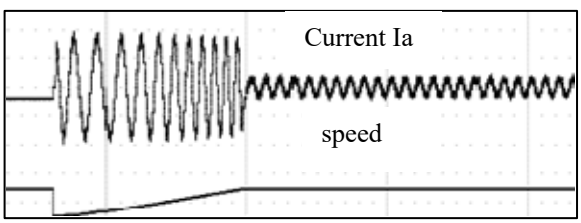

(c)

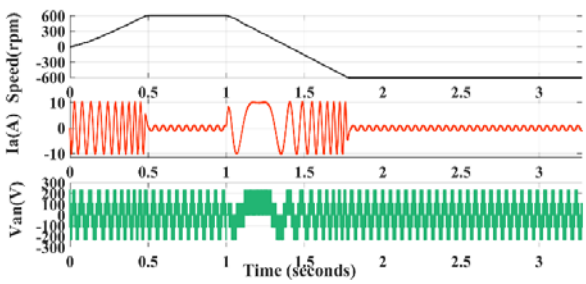

(d)

Fig. 16. (a) Phase currents; (b) speed, phasecurrent and load torque of the proposed hysteresis controller based IM drive at 20 Hz during a load change; (c) phase current and speed of the proposed CC IM drive when accelerating from standstill to 20 Hz, [Y:upper trace:1 div=2.5 A, lower trace:1 div=50 rad/sec, X:1 div=0.50s]; (d) speed reversal of an IM drive using the proposed CC from 20Hz to -20Hz.

demonstrated results manifested a serene steady state and dynamic performance throughout the changeovers with the switching frequency fluctuation control.

V. Comparison of Controllers

Current control techniques for VSIs give better control of the current waveforms and provide compensation for load transients when compared to VC VSI fed IM drives. However,

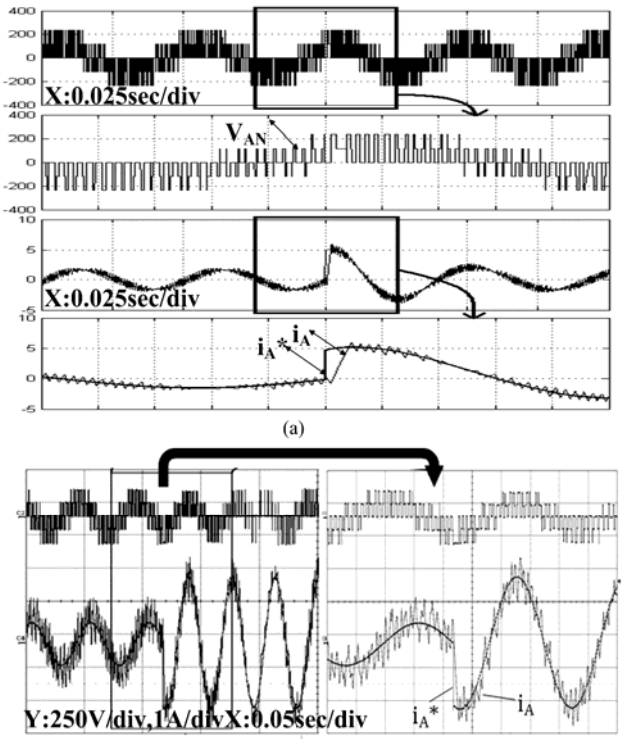

(a) (b)

Fig. 17. Expanded and zoomed version of phase voltage, phase current and reference current at 20 Hz, when a sudden change in Isq is applied with the proposed CC IM drive: (a) simulated results; (b) experimental results.

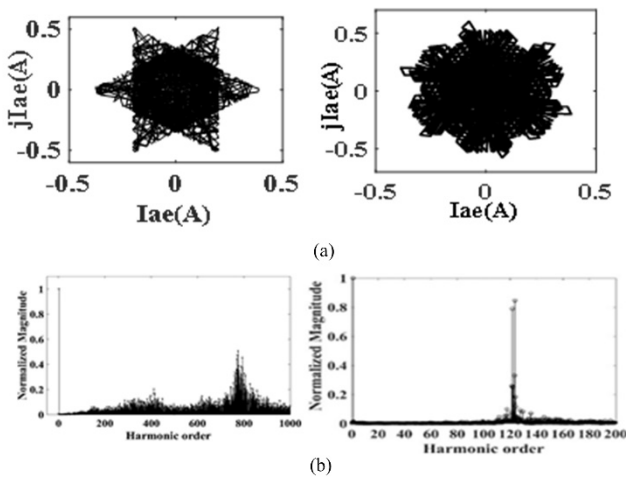

(a) (b)

Fig. 18. (a) CESP in one cycle [Y:0.5A/div; X:0.5A/div]; (b) normalized harmonic spectrum of the phase voltage at 10 Hz (X: Harmonic order; Y: Normalized harmonic amplitude) in the conventional HCC and in the proposed CC.

the magnitude of the CESP can become double the hysteresis band in conventional HCC as in the Fig. 18.a results in high frequency switching. This is eliminated in the proposed controller.

From the normalized harmonic spectrum of the phase voltage, shown in Fig.18.b, it is clear that the switching frequency in the conventional HCC varies from 2 KHz to 10 KHz, whereas a nearly constant switching frequency of 1250

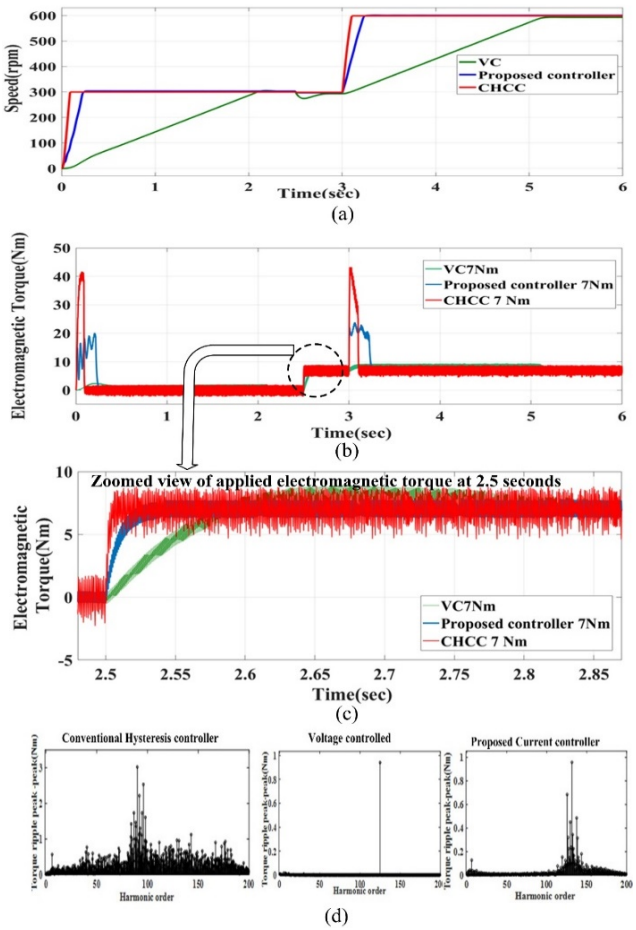

Fig. 19. (a) Simulations for the VC, the conventional HCC and the proposed CC during the acceleration of an IM from 10 Hz to 20 Hz with a load torque of 7 Nm applied at 2.5 sec and a speed change applied at 3 sec [Y:100rpm/div,X:1sec/div]. (b) Variations of the electromagnetic torque developed at 2.5 sec in the VC, the conventional HCC and the proposed CC VSI fed IM drive [Y:10Nm/div; X:1sec/div]. (c) Zoomed view of electromagnetic torque applied at 2.5 sec. (d) Harmonic spectrum of the torque ripple for the conventional HCC, the VC and the proposed CC obtained in Fig. 19(c).

Hz is achieved in the CESP based proposed controller. Therefore, the hysteresis controller is formulated so that the voltage generated at the output of the inverter has a frequency spectrum that is similar to that of the constant switching frequency VC-SVPWM as in Fig. 9(a). In addition, Fig. 19(a) shows the acceleration transients of an IM from 10 Hz to 20 Hz with a load torque of 7 Nm applied at 2.5 sec using the Voltage Controlled (VC), the conventional HCC and the proposed CC method. Fig. 19(b) gives the electromagnetic torque developed at 2.5 sec in the VC, the conventional HCC and the proposed CC IM drive. Fig. 19(c) shows the zoomed electromagnetic torque variation in the VC, the conventional HCC and the proposed CC. The harmonic spectrum of the torque ripple is carried out for the above mentioned controllers as shown in Fig. 19(d). The switching frequency is almost consistent with the frequency of the torque ripple.

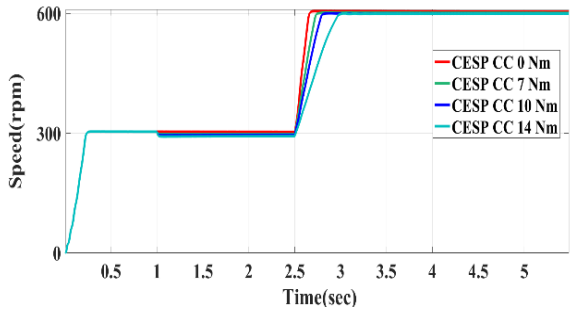

Fig. 20. Proposed CC VSI fed IM drive during acceleration from 10 Hz to 20 Hz with various load torques applied at 1 sec and a speed change applied at 2.5 sec [Y:300rpm/div; X:0.5sec/div].

TABLE IV
COMPARISON OF CONTROLLERS

	Voltage Control(VC)	Conventional Hysteresis current control(CHCC)	Proposed CESP Based control(CC)
Switching frequency	Constant (1250 Hz)	Variable (2KHz-10 KHz)	Nearly Constant (1220Hz-1260 Hz)
Dynamic Response	Inferior	Superior	Superior
Rise Time	2.1 s	100ms	235ms
Settling Time	350ms	40ms	60ms

Constant, variable and nearly constant switching frequency are obtained in the VC, the conventional HCC and the proposed current controlled IM drives, respectively.

Fig. 20 shows the fast dynamic response of the proposed controller with various load torques applied at 1 sec. A comparison between the controllers has been done in terms of switching frequency, dynamic response, rise time and settling time as in Table IV. Here the settling time is defined as the time taken to bring back the machine torque to the steady state rated torque after a sudden load change is applied. It is noted that the proposed controller has a better dynamic response than the VC-VSI fed IM. Thus, the advantages of both the CHCC and the VC can be integrated into one. A theoretical comparison of the CHCC, the existing predictive and dead beat control, the CESP based control, etc. has been carried out and presented in Table V. It is observed that the proposed control offers better benefits than the other existing current control strategies.

VI. CONCLUSION

This paper proposes a simple and fast online computed current error boundary based nearly constant switching frequency hysteresis current controller for 2 level VSI fed IM drives. The varying hysteresis boundary is formulated based on instantaneous measured fundamental stator voltages along the alpha and beta axes. Experimentation results are presented for different operating speeds of the machine and their matching

TABLE V
THEORETICAL COMPARISON OF CURRENT CONTROLLERS

Current control strategy	Parameters used for comparison with justification				
	Methodology /Control	**Main features**	**Switching frequency**	**Drawbacks**	**Applications**
Conventional Hysteresis current controller (CHCC) [1]	Comparison of machine current and reference current within the bands	Fast dynamic response Easy implementation Inherent peak current limiting	Variable over a wide speed range	Switching frequency variations when current exceeds band Generate sub harmonic current	Inverter-based drives and high ac power application, active power filter
Hysteresis based Predictive Control [2]	Prediction and calculation of optimum vector for switching in every sampling period	Quick and accurate response	Minimum switching frequency variation	Extensive computation and complex implementation	Direct speed control, machine control
Dead beat based predictive control [2], [3]	Reference voltage generated using current comparison is applied to modulator for generating inverter switching sequence	Low computation Fast dynamic response Better current waveform	Fixed switching frequency	Instability issues during nonlinearity and transients	Current control inverter, active filter, UPS, dc–dc converters, drives
Current Error Space Phasor(CESP)based HC with varying parabolic boundary [7]-[9]	When CESP goes outside boundary a voltage vector which will bring back the error inside the boundary will be switched	Reduced switching frequency variation Good dynamic response	Reduced switching frequency variation	Switching frequency variations over a wide speed range Offline data storage for computations	Active filters, three phase inverters
CESP based HC with online boundary computation (proposed control)	Current error along orthogonal axis monitored for vector selection	Nearly constant switching frequency Good transient & dynamic performance	Constant switching frequency for entire speed range of operation		Current control inverter, inverter-based drives and high ac power applications

with the simulation results is demonstrated to verify the concept of a constant switching frequency using online variation of the current error boundaries. Adjacent vector switching and a fast dynamic response are achieved in the presented scheme in addition to the elimination of switching frequency variations.

APPENDIX

Motor data: 3 Phase, 2.2 kW, star connected, 4 poles, 415V, 1440rpm, R_s=4.8Ω, R_r=3.8Ω, L_s=0.5632H, L_r=0.577H, M=0.546H, and Rated Torque=14Nm.

REFERENCES

[1] D. M. Brod and D. W. Novotny, "Current control of VSI-PWM inverters," *IEEE Trans. Ind. Appl.*, Vol. IA-21, No. 4, pp. 562-570, May/Jun. 1985,

[2] M. P. Kazmierkowski, and L. Malesani, "Current control techniques for three phase voltage-source PWM converters: a survey," *IEEE Trans. Ind. Electron.*, Vol. 45, No. 5, pp. 691-703, Oct. 1998.

[3] I. Nagy, "Novel adaptive tolerance band based PWM for field-oriented control of induction machines," *IEEE Trans. Ind. Electron.*, Vol. 41, No. 4, pp.406-417, Aug. 1994.

[4] K. Bose, "An adaptive hysteresis- band current control technique for a voltage fed PWM inverter for machine drive system," *IEEE Trans. Ind. Electron.*, Vol. 37, No. 5, pp. 402-408, Oct. 1990.

[5] G. Fernandes, S. K. Pillai, and V. Subbarao, "Digital simulation of an adaptive hysteresis current controlled induction motor drive," in *Proc. IEEE-ISCAS-1992, 3-6* Vol. 2, pp. 923-926, May 1992.

[6] V. Mistry, S. P. Waiker, K. Gopakumar, L. Umanand, and V. T. Ranganathan, "A multi axis space vector based current hysteresis controller for PWM Inverters," *EPE Journal*, Vol. 10, No. 1, pp. 17-25, Apr. 2000.

[7] M. R. Baiju, K. K. Mohapatra, R. S. Kanchan, P. N. Tekwani, and K.Gopakumar, "A space vector based current hysteresis controller using adjacent inverter voltage vectors with smooth transition to six step operation for a three phase voltage source inverter," *EPE Journal*, Vol. 15, No. 1, pp. 36-47, Feb. 2005.

[8] P. N. Tekwani, R. S. Kanchan, and K. Gopakumar, "Novel currenterror space vector based hysteresis controller using parabolic bands for control of switching frequency variations," *IEEE Trans. Ind.Electron.,* Vol. 54, No. 5, pp. 2648-2656, Oct. 2007.

[9] R. Ramchand, K. Sivakumar, A. Das, C. Patel, and K. Gopakumar, "Improved switching frequency variation control of hysteresis controlled voltage source inverter-fed IM drives using current error space vector," *IET Power Electron*., Vol. 3, No. 2, pp. 219-231, Mar. 2010.

[10] R. Ramchand, C. Patel, K. Sivakumar, A. Das, and H. Abu-Rub, and K. Gopakumar, "Online computation of hysteresis boundary for constant switching frequency current error space vector based hysteresis controller for VSI fed IM drives," *IEEE Trans. Power Electron.*, Vol. 27, No. 3, pp. 1521 - 1529, Mar. 2012.

[11] N. A. Azeez, A. Dey, K. Mathew, J. Mathew, K. Gopakumar, and M. P. Kazmierkowski,

"A medium-voltage inverter-fed IM drive using multilevel 12-sided polygonal vectors, with nearly constant switching frequency current hysteresis controller," *IEEE Trans. Ind. Electron.*, Vol. 61, No. 4, pp. 1700-1709, Apr. 2014.

[12] H. Yi, F. Zhuo, F. Wang, and Z. Wang, "A digital hysteresis current controller for three-level neural-point-clamped inverter with mixed-levels and prediction-based sampling," *IEEE Trans. Power Electron.*, Vol. 31, No. 5, pp. 3945-3957, May 2016.

[13] A. Dey, N. A. Azeez, K. Mathew, K. N. Gopakumar, and M. P. Kazmierkowski, "Hysteresis current controller for a general η-level inverter fed drive with online current error boundary computation and nearly constant switching frequency," *IET Power Electron.*, Vol. 6, No. 8, pp. 1640-1649, Sep. 2013.

[14] A. Dey, P. P. Rajeevan, R. Ramchand, K. Mathew, and K. Gopakumar, "A space-vector-based hysteresis current controller for a general n-level inverter-fed drive with nearly constant switching frequency control," *IEEE Trans. Ind. Electron.*, Vol. 60, No. 5, pp. 1989-1998, May 2013.

[15] A. Bozicek, B. Blazic, and I. Papic, "Performance evaluation of a time-optimal current controller for a voltage-source converter and comparison with a hysteresis controller," *IEEE Trans. Power Del.*, Vol. 26, No. 2, pp. 859-868, Apr. 2011.

[16] K. Basu, J. S. S. Prasad, G. Narayanan, H. K. Krishnamurthy, and R. Ayyanar, "Reduction of torque ripple in induction motor drives using an advanced hybrid PWM technique," *IEEE Trans. Ind. Electron.*, Vol. 57, No. 6, pp. 2085-2091, Jun. 2010.

[17] G. Narayanan, D. Zhao, H. K. Krishnamurthy, R. Ayyanar, and V. T. Ranganathan, "Space vector based hybrid PWM techniques for reduced current ripple," *IEEE Trans. Ind. Electron.*, Vol. 55, No. 4, pp. 1614-1627, Apr. 2008.

[18] J. Peter and R. Ramchand, "A current error space phasor based hysteresis controller for voltage source inverter fed induction motor drive," *2015 IEEE International Conference on Signal Processing, Informatics, Communication and Energy Systems (SPICES)*, pp. 1-5, 2015.

Joseph Peter received his B. Tech degree in Electrical and Electronics Engineering from Mar Athanasius College of Engineering, Kothamangalam, Kerala, India, in 2009; and his M. Tech degree in Power Electronics and Drives from VIT University, Vellore, Tamil Nadu, India, in 2012. He is presently working towards his Ph.D. degree at the National Institute of Technology, Calicut, Kerala, India. His current research interests include pulse width modulation techniques and current controlled ac drives.

Mohammed Shafi K P received his B. Tech. degree in Electrical and Electronics Engineering from the Cochin University of Science and Technology, Kerala, India, in 2013; and his Master degree in Power Electronics from the National Institute of Technology, Calicut, Kerala, India, in 2016, where he is presently working towards his Ph.D. degree. His current research interests include pulse width modulation techniques and control for ac drives.

Rijil Ramchand received his B. Tech. degree in Electrical and Electronics Engineering from Calicut University, Calicut, India, in 1996; and his M.E. and Ph.D. degrees from the Indian Institute of Science, Bangalore, India, in 2002 and 2010, respectively. He is presently working as an Associate Professor in the Department of Electrical Engineering, National Institute of Technology, Calicut, India. His current research interests include power converters, pulse width modulation techniques, multilevel inverters and current controlled ac drives. He is a senior member of IEEE.